Electronic Supplementary Information

Metal-metalloporphyrin MOF-derived core-shell Ni_3Fe@FeNi-NC towards high-performance bifunctional oxygen electrocatalysis

Kairen Cheng,[a] Guoxin Zhang,[a] Xingxing Li,[a] Jiangxia Tian,[a] Min Zhao,[b] Kai Chen,*[a] Aili Liu,*[a] Shun Wang[a] and Huile Jin*[a]

[a] Wenzhou Key Lab of Advanced Energy Storage and Conversion, College of Chemistry and Materials Engineering, Wenzhou University, Wenzhou, Zhejiang 325035, China.

[b] Jinhua Advanced Research Institute, Jinhua, Zhejiang, 321017, China.

Corresponding authors: Kai Chen, kaichen@wzu.edu.cn;

Aili Liu, ailikeji@126.com;

Huile Jin, huilejin@wzu.edu.cn.

Experimental Section

1. Chemicals and Materials

Pyrrole and methyl *p*-formylbenzoate were purchased from Shanghai Bide Pharmatech Co., Ltd. Ferrous chloride tetrahydrate ($FeCl_2 \cdot 4H_2O$), Ferric chloride hexahydrate ($FeCl_3 \cdot 6H_2O$), nickel chloride hexahydrate ($NiCl_2 \cdot 6H_2O$), 2,5-dihydroxyterephthalic acid, tetrahydrofuran (THF), concentrated hydrochloric acid (HCl), concentrated sulfuric acid (H_2SO_4), sodium hydroxide (NaOH), potassium hydroxide (KOH), zinc acetate dihydrate ($Zn(OAc)_2 \cdot 2H_2O$), nickel nitrate hexahydrate ($Ni(NO_3)_2 \cdot 6H_2O$), pyrazine, ethanol (EtOH), *N, N*-dimethylformamide (DMF), methanol (MeOH), were purchased from Sinopharm Group Co., Ltd. Pt/C (20 wt%), RuO_2, Nafion solution and carbon black were purchased from Suzhou Sinero Tech Co., Ltd. Zinc foil, composite electrode (made of hydrophobic carbon paper and electronic conductor), customized ZAB device (OMS-TR1) were purchased from Changsha Spring New Energy Technology Co., Ltd. All chemicals and materials were used as received without further purification.

2. Preparation of MOF precursors.

[5,10,15,20]-Tetrakis(4-carboxyphenyl)porphine-Fe(III) chloride (FeTCPP) was synthesized according to the reference.[1] Bulk Ni-FeTCPP was prepared based on the previous report without modification.[2] Briefly, $Ni(NO_3)_2 \cdot 6H_2O$ (5.8 mg), FeTCPP (8.8 mg), pyrazine (1.6 mg), DMF (1.5 mL), and ethanol (0.5 mL) were added into a small capped vial, and heated at 80 °C for 24 h. The resulting dark purple Ni-FeTCPP solids were harvested by centrifugation, washed thoroughly with ethanol, and dried at 80 °C overnight.

The synthesis of Zn-Fe/NiTCPP, Zn-FeTCPP, and Zn-NiTCPP was similar to Ni-FeTCPP by replacing the FeTCPP with FeTCPP (4.4 mg) and NiTCPP (4.4 mg), FeTCPP (8.8 mg), and NiTCPP (8.8 mg), respectively.

NiFe-MOF was synthesized according to the reference.[3] Concretely, $NiCl_2 \cdot 6H_2O$ (1,114 mg, 4.69 mmol), $FeCl_3 \cdot 6H_2O$ (421 mg, 1.56 mmol), and 2,5-dihydroxyterephthalic acid (416 mg, 2.1 mmol) were added to in 150 mL DMF-ethanol-H_2O (1:1:1) mixed solution and sonicated till complete dissolution. The mixture was transferred to a Teflon-lined stainless-steel autoclave and heated in oven at 120 °C for 24 h. After cooling down to room temperature, the solid was harvested

by filtration and washed thoroughly with DMF and ethanol. Finally, the solid residue was further dried at 80 °C overnight to afford NiFe-MOF.

3. Preparation of MOF-derived carbon materials

The obtained Ni-FeTCPP was pyrolyzed at 900 °C in a nitrogen atmosphere for 2 h at a ramping rate of 5 °C min^{-1} to afford Ni_3Fe@FeNi-NC.

The synthesized Zn-Fe/NiTCPP, Zn-FeTCPP, and Zn-NiTCPP were first pyrolyzed at 900 °C and then etched by 0.5 M H_2SO_4 solution at 80 °C for 24 h. The black powder was filtered and washed thoroughly with deionized water till neutral to afford FeNi-NC, Fe-NC, and Ni-NC, respectively.

Ni_3Fe@C was prepared by direct pyrolysis of NiFe-MOF at 900 °C.

Ni_3Fe + FeNi-NC was synthesized by integrating the Ni_3Fe@C and FeNi-NC components [4]. 100 mg Ni_3Fe@C and 100 mg FeNi-NC were added and dispersed into 50 mL ethanol to form a homogeneous suspension under continuous stirring at room temperature for 24 h. The hybrid product was separated by filtration and washed with deionized water and ethanol for three times, respectively. Finally, Ni_3Fe + FeNi-NC was obtained after drying at 60 °C overnight.

4. Characterization

Scanning electron microscopy (SEM) images were performed on a NoVa 200 NanoLab (FEI). High-resolution transmission electron microscopy (HR-TEM) images were collected on JEM-2100F (JEOL). Powder X-ray diffraction (PXRD) patterns were recorded on a D8 Advance (Bruker) with filtered Cu Kα radiation (λ = 1.5406 Å, operating at 40 kV and 40 mA). The nitrogen adsorption-desorption measurements were performed on a BELSORP mini II (BEL Inc.). The specific surface area was calculated using the Brunauer-Emmett-Teller (BET) model in the relative pressure range between 0-0.5. X-ray photoelectron spectra (XPS) were collected on a K-Alpha (Thermo Scientific), performing at 15 kV and 15 mA with a monochromatic Al Kα source (hv = 1486.71 eV). Raman spectra were recorded on a Renishaw inVia Raman spectrometer with excitation from the 532 nm line of an Ar-ion laser.

5. Electrochemical measurements

All electrochemical measurements were performed using a CHI-760E electrochemical workstation (Shanghai Chenhua Instrument Co., China) in a three-electrode cell. A catalyst-loaded rotating disk electrode (RDE) (PINE) or rotating ring-disk electrode (RRDE) (PINE) was used as a working electrode, an Ag/AgCl (saturated KCl) electrode, and a graphite rod was utilized as reference and counter electrode, respectively. All the potentials were calibrated to the reversible hydrogen electrode (RHE) according to the Nernst equation:

$$E_{RHE} = E_{Ag/AgCl} + 0.0592 \times pH + E^{\ominus}_{Ag/AgCl}$$

The catalyst ink was prepared by dispersing 6.0 mg of the as-synthesized catalyst and 4.0 mg of carbon black in a mixed solution containing 980 μL of ethanol and 20 μL of 5 wt% Nafion solution, followed by ultrasonication until a homogeneous dispersion was observed. A specific volume of the catalyst ink was then pipetted onto the working electrode to obtain a catalyst loading of 0.6 mg·cm^{-2}. The ORR measurements were performed in an O_2-saturated 0.1 M KOH electrolyte within a potential range of 0-1.1 V *vs.* RHE at a scan rate of 10 mV s^{-1}. The stability of the electrocatalyst was assessed using chronoamperometry at 0.5 V *vs.* RHE. The methanol tolerance of the catalyst was evaluated by adding 10 mL of methanol to the electrolyte. RDE measurements were conducted at different rotating speeds ranging from 625 to 2500 rpm, with a cathodic scan rate of 5 mV s^{-1}. The electrochemical impedance spectroscopy (EIS) measurements were carried out in the frequency range of 0.01 to 100 kHz and potential amplitude of 5 mV.

The electron transfer number (n) was calculated by Koutecky-Levich equation:

$$\frac{1}{j} = \frac{1}{j_l} + \frac{1}{j_k} = \frac{1}{B\omega^{1/2}} + \frac{1}{j_k}$$

$$B = 0.62nF\,C_0\,(D_0)^{2/3}\,v^{-1/6}$$

$$j_k = nFkC_0$$

where j is the measured current density; j_k and j_l are the kinetic and diffusion limiting current densities, respectively; ω is the angular velocity of the rotating electrode ($\omega = 2\pi N$, where N is the linear rotation speed); F is the Faraday constant (F = 96,485 C mol^{-1}); C_0 is the saturated concentration of O_2 in 0.1 M KOH (1.2×10^{-3} M); D_0 is the diffusion coefficient of O_2 in 0.1 M KOH (1.9×10^{-5} cm^2 s^{-1}); v is the kinematic viscosity of the electrolyte (0.01 cm^2 s^{-1}), and k is the electron transfer rate constant.

The RRDE tests were scanned cathodically at a rate of 5 mV·s^{-1}. The H_2O_2 yield (%) and the electron transfer number (n) were calculated by the following equations:

$$n = \frac{4I_{disk}}{I_{disk} + \frac{I_{ring}}{N}}$$

$$(H_2O_2)\% = \frac{200 \times \frac{I_{ring}}{N}}{I_{disk} + \frac{I_{ring}}{N}}$$

where I_{disk} and I_{ring} are the disk current and ring current, respectively; N is the current collection efficiency of 0.37 for the Pt ring.

6. Aqueous zinc-air batteries (ZABs) tests.

The electrochemical performance of the catalysts was evaluated in a custom-built ZAB system, integrated with a multichannel potentiostat for comprehensive single-cell characterization. In a typical ZAB, a polished Zn foil served as the anode, a catalyst-loaded composite electrode served as the cathode, and a mixed solution containing 6 M KOH and 0.2 M $Zn(OAc)_2$ was utilized as the electrolyte. The active area of the Zn anode and air cathode were 4.5 cm^2 and 0.4 cm^2, respectively. The total volume of electrolyte in the chamber was 5 mL, and the flow rate of the electrolyte was maintained at 20 mL min^{-1}. The catalyst ink was prepared by the same method in the three-electrode system, with the catalyst loading on the composite electrode being approximately 1.2 mg cm^{-2}.

Results and Discussion

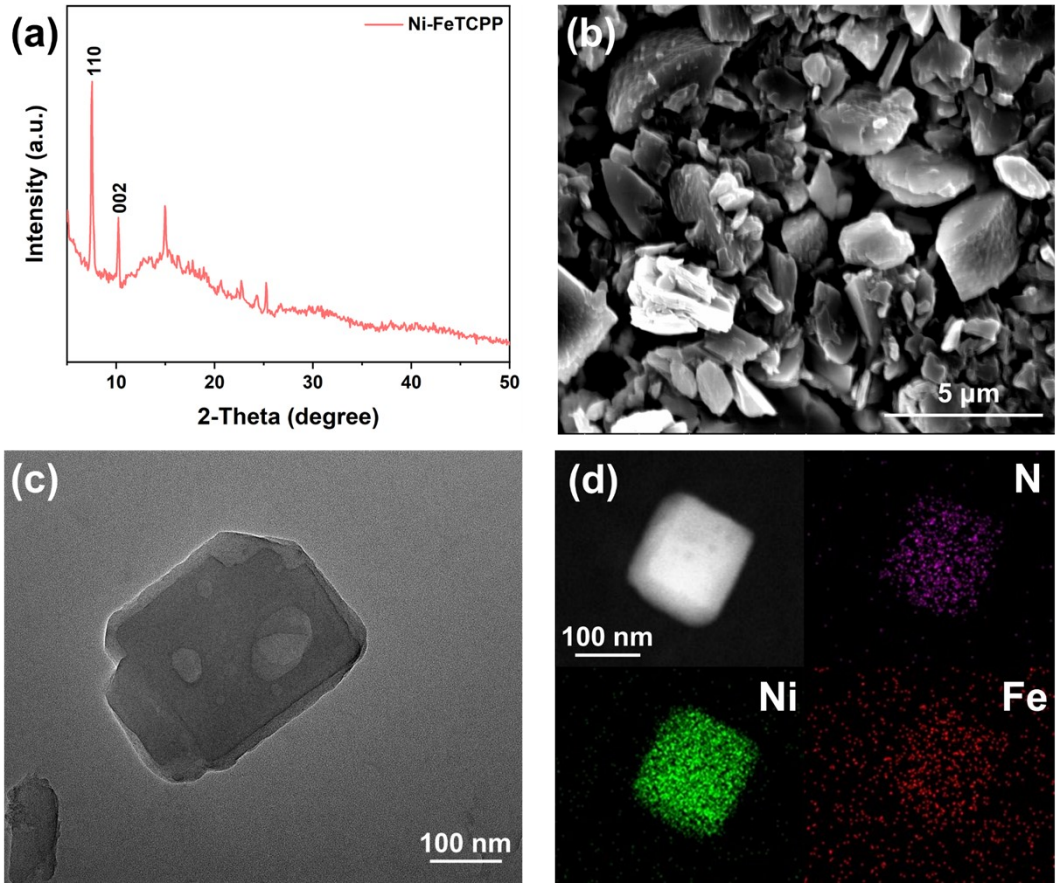

Fig. S1 (a) PXRD pattern, (b) SEM image, (c) TEM image, and (d) corresponding EDS elemental mapping images of Ni-FeTCPP.

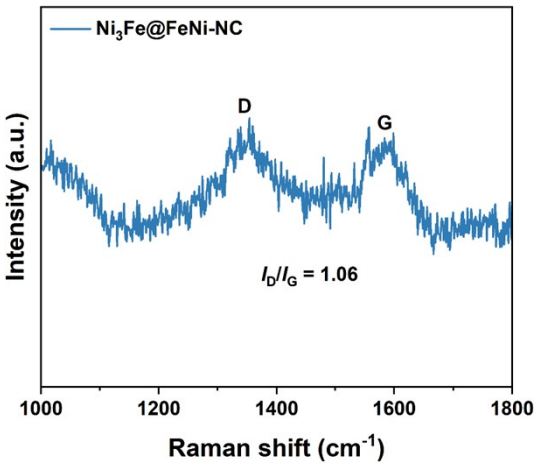

Fig. S2 Raman spectrum of Ni_3Fe@FeNi-NC.

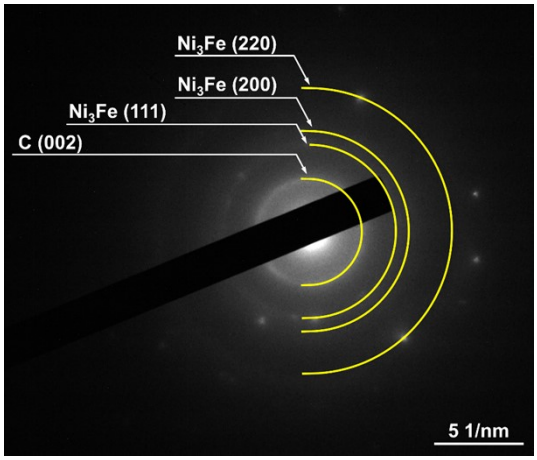

Fig. S3 Selected area electron diffraction (SAED) pattern of Ni_3Fe@FeNi-NC.

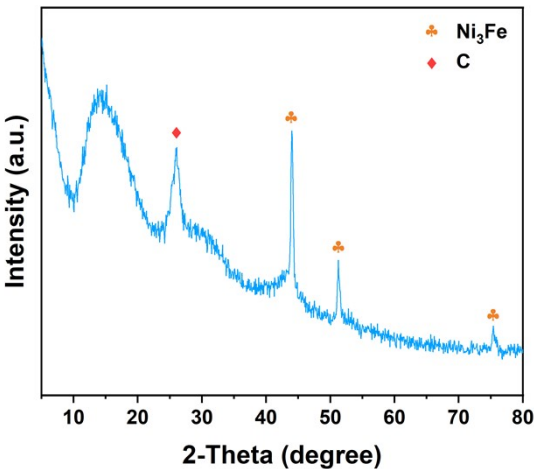

Fig. S4 PXRD pattern of Ni_3Fe@FeNi-NC after etching in 0.5 M H_2SO_4 solution at 80 °C for 24 h.

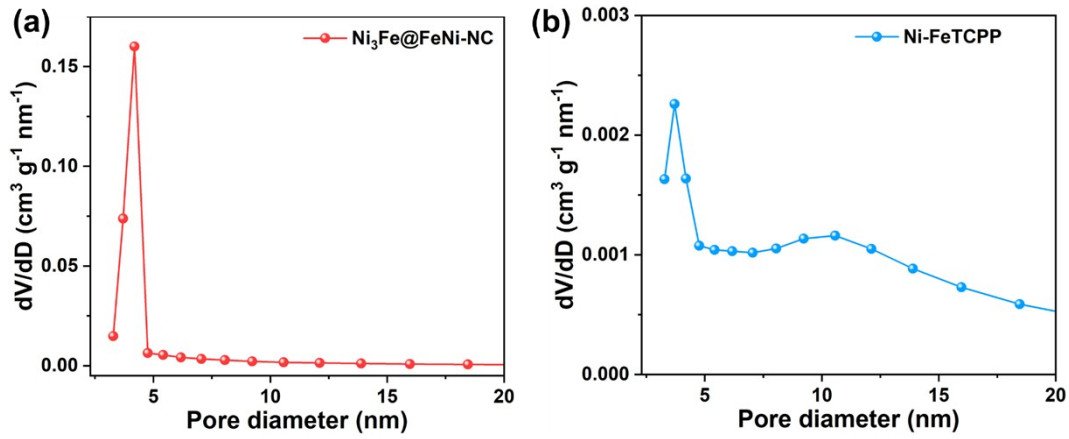

Fig. S5 Pore size distribution curves of (a) Ni_3Fe@FeNi-NC and (b) Ni-FeTCPP.

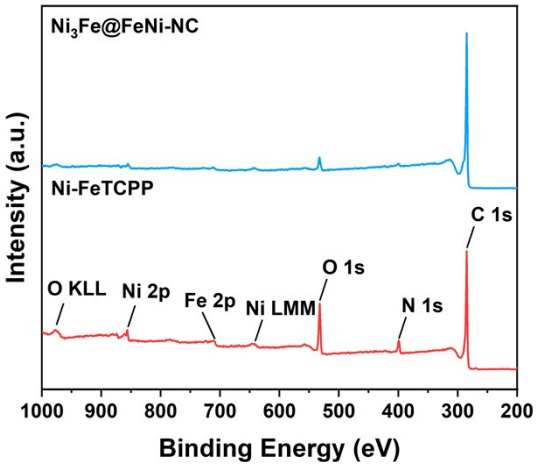

Fig. S6 XPS survey spectra of Ni_3Fe@FeNi-NC and Ni-FeTCPP.

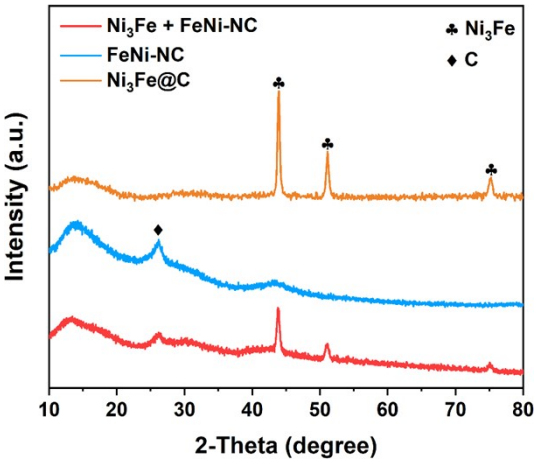

Fig. S7 PXRD patterns of (a) Ni_3Fe@C, (b) FeNi-NC, and (c) Ni_3Fe + FeNi-NC.

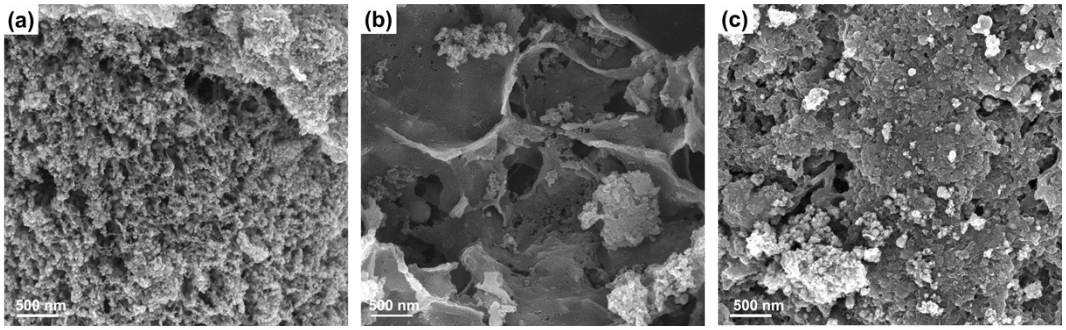

Fig. S8 SEM images of (a) Ni_3Fe@C, (b) FeNi-NC, and (c) Ni_3Fe + FeNi-NC.

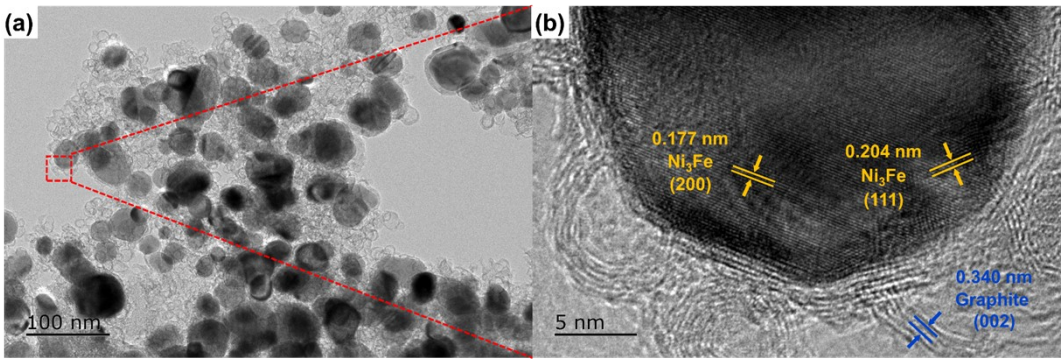

Fig. S9 HRTEM images of Ni_3Fe + FeNi-NC.

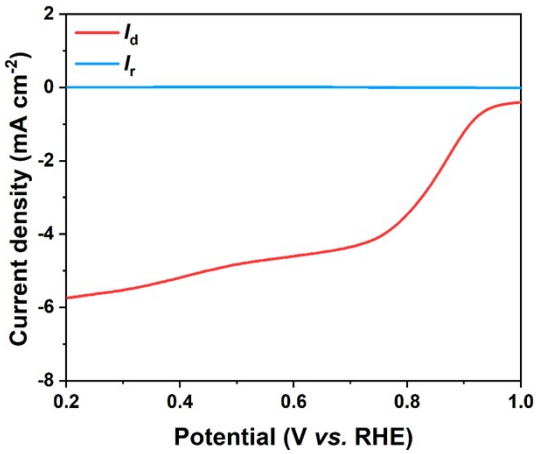

Fig. S10 RRDE voltammograms of Ni_3Fe@FeNi-NC in 0.1 M KOH solution at 1600 rpm.

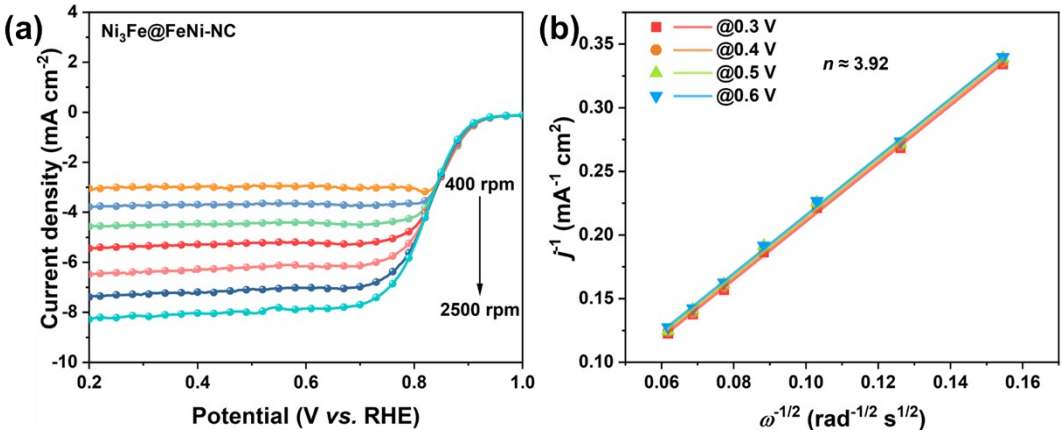

Fig. S11 ORR polarization curves at various rotation rates and corresponding Koutecky-Levich plots for Ni_3Fe@FeNi-NC.

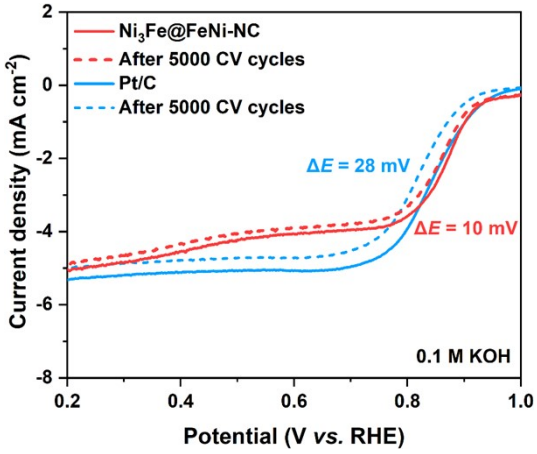

Fig. S12 ORR polarization curves of Ni_3Fe@FeNi-NC and Pt/C after the 5,000 cycle.

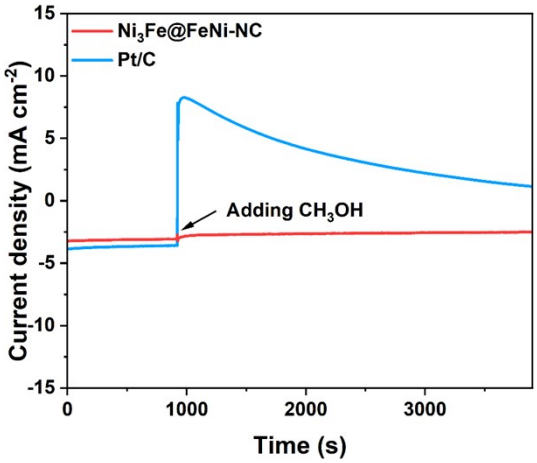

Fig. S13 Methanol tolerance tests for Ni_3Fe@FeNi-NC and Pt/C in O_2-saturated 0.1 M KOH solution with the addition of methanol.

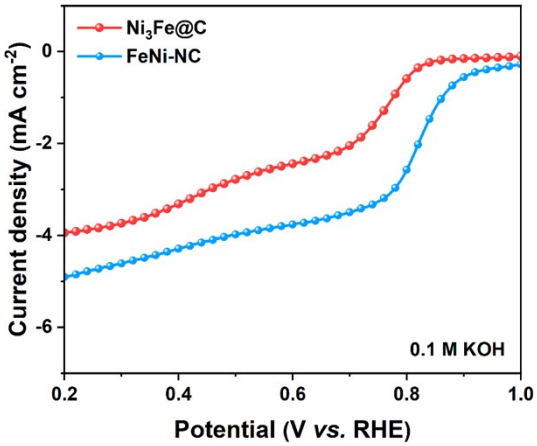

Fig. S14 ORR polarization curves of Ni_3Fe@C and FeNi-NC in O_2-saturated 0.1 M KOH solution.

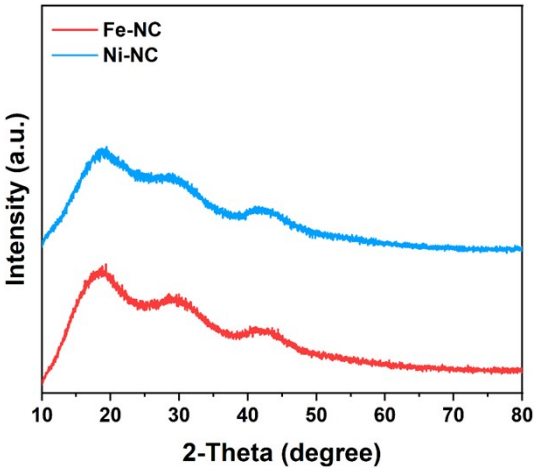

Fig. S15 PXRD patterns of Fe-NC and Ni-NC.

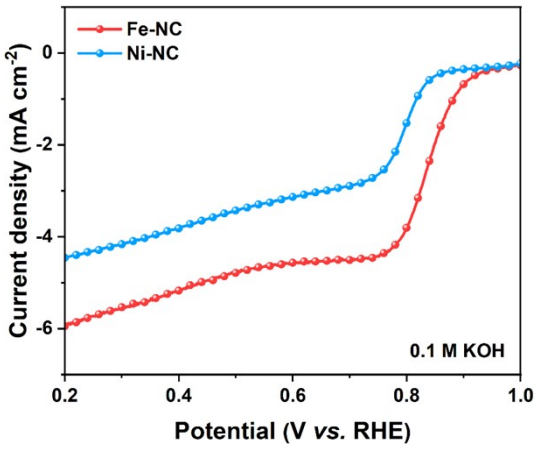

Fig. S16 ORR polarization curves of Fe-NC and Ni-NC in O_2-saturated 0.1 M KOH solution.

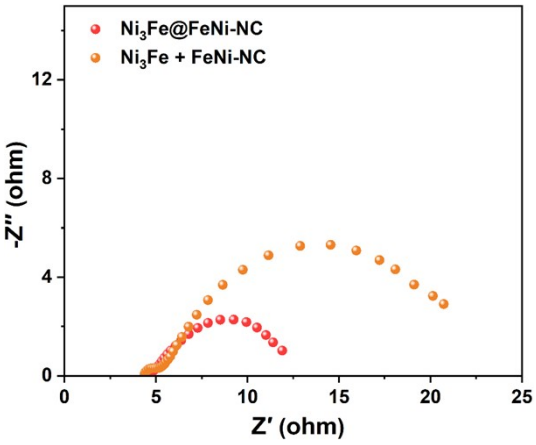

Fig. S17 Electrochemical impedance spectra of Ni_3Fe@FeNi-NC and Ni_3Fe + FeNi-NC.

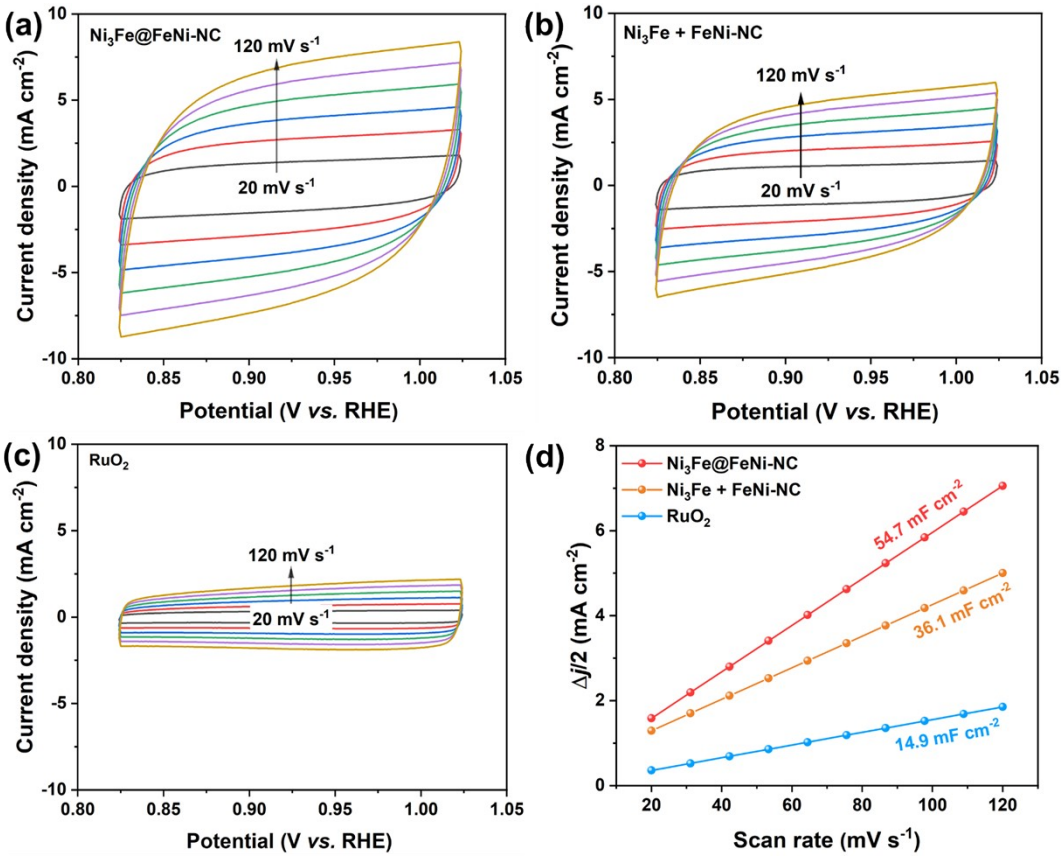

Fig. S18 Cyclic voltammograms recorded at different scan rates for (a) Ni_3Fe@FeNi-NC, (b) Ni_3Fe + FeNi-NC, and (c) RuO_2, respectively. (d) Corresponding fitted C_{dl} plots.

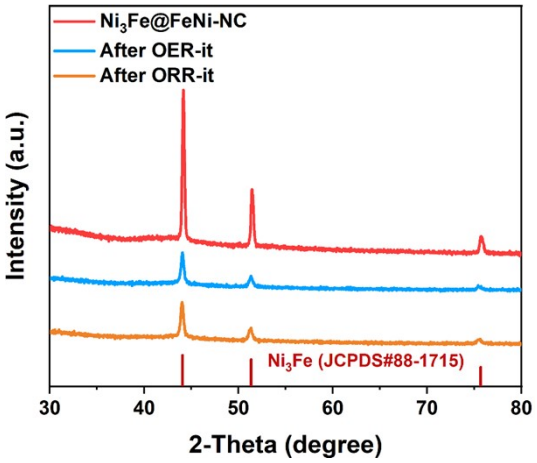

Fig. S19 PXRD patterns of Ni_3Fe@FeNi-NC after ORR and OER chronoamperometric tests.

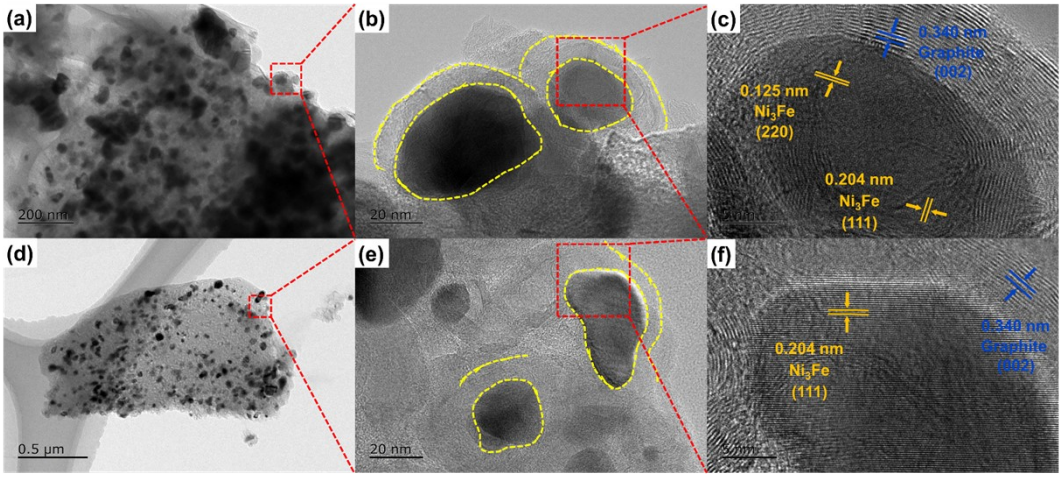

Fig. S20 HRTEM images of Ni_3Fe@FeNi-NC after (a-c) ORR and (d-f) OER chronoamperometric tests.

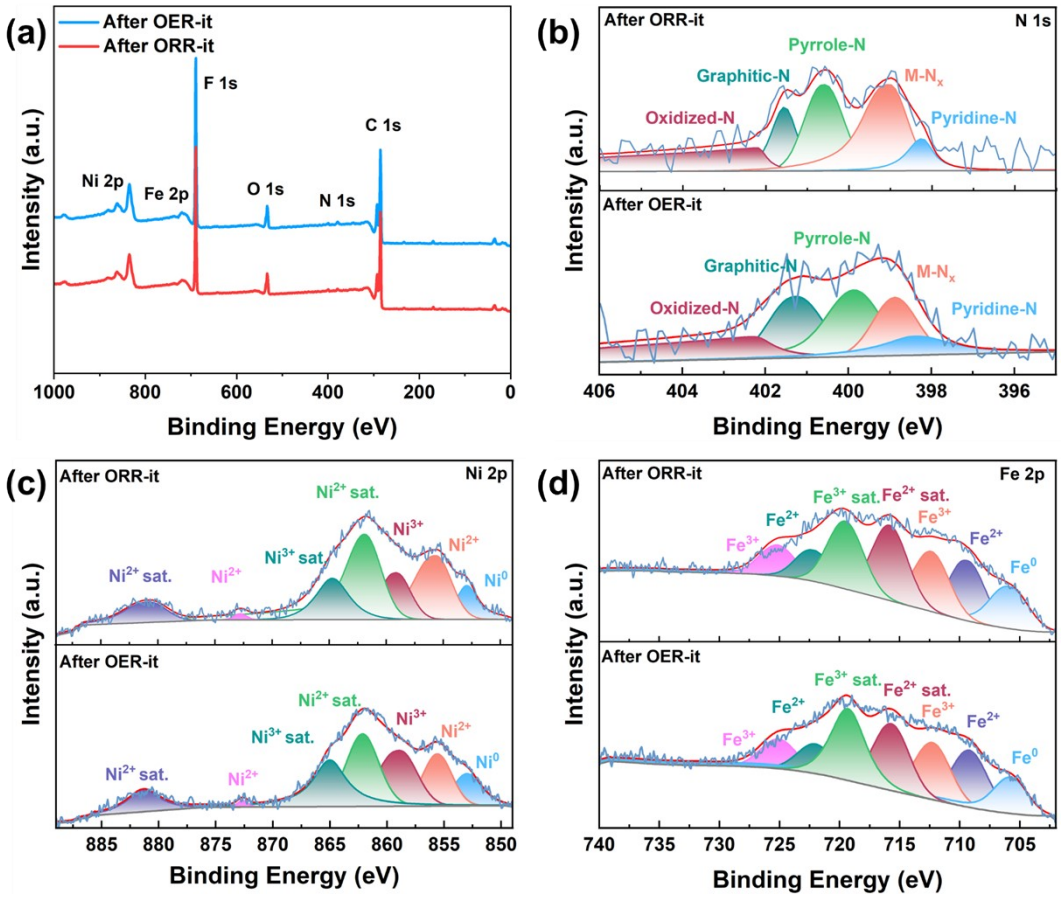

Fig. S21 (a) Survey, (b) N 1s, (c) Ni 2p, and (d) Fe 2p high-resolution XPS spectra of Ni_3Fe@FeNi-NC after ORR and OER chronoamperometric tests. The abnormal Ni 2p spectra resulted from the confusion with F KLL Auger electron transition of fluorine from the commonly used Nafion binder, when the XPS spectra are acquired with Al Kα X-ray source.[5]

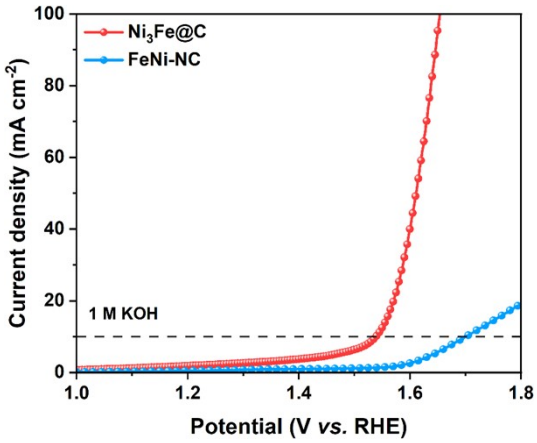

Fig. S22 OER polarization curves of Ni_3Fe@C and FeNi-NC in O_2-saturated 1.0 M KOH solution.

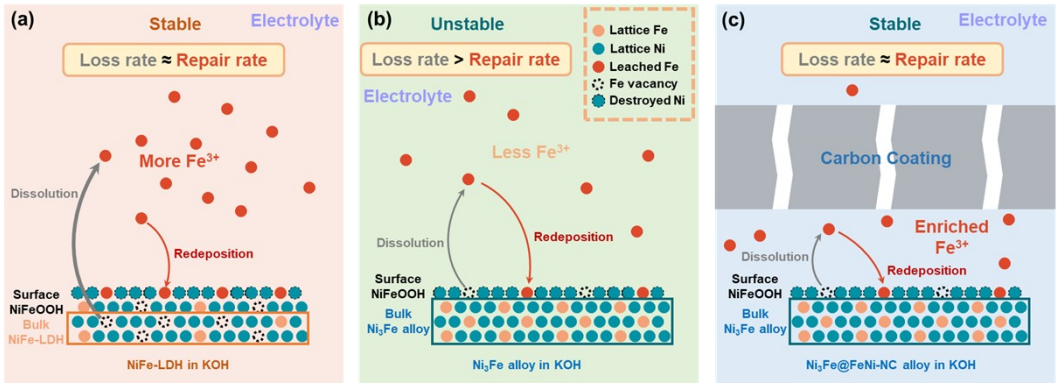

Fig. S23 Schematic diagram of the Fe dissolution and redeposition for (a) NiFe-LDH, (b) Ni_3Fe alloy, and (c) Ni_3Fe@FeNi-NC in KOH during the OER process.[6]

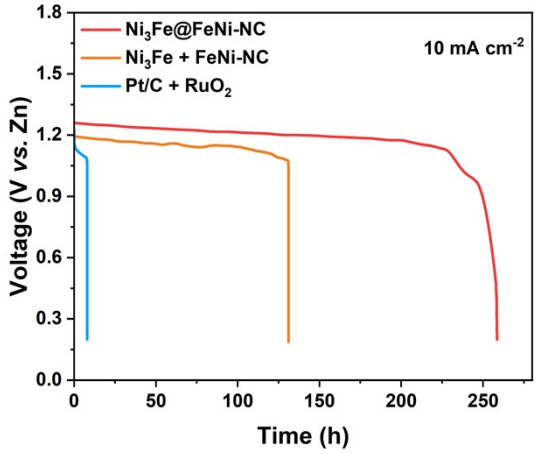

Fig. S24 Galvanostatic discharging profiles of various catalyst-assembled zinc-air batteries at 10 mA cm^{-2}.[7] The Ni_3Fe@FeNi-NC-based ZAB delivered superior discharge capability and long-term stability.

Table S1. Elemental contents of C, N, Ni, and Fe in Ni-FeTCPP and Ni_3Fe@FeNi-NC.

Sample	Chemical composition (at%)[a]				Metal content (wt%)	
	C	N	Ni	Fe	Ni	Fe
Ni-FeTCPP	87.42	8.57	2.46	1.55	-	-
Ni_3Fe@FeNi-NC	89.88	1.8	3.24	5.08	21.7	8.6

[a] The atomic contents were collected from XPS analysis;

[b] The metal content was determined by the ICP-OES method.

Table S2 Comparison of ORR and OER bifunctional catalytic activities between Ni_3Fe@FeNi-NC and reported well-developed transition-metal electrocatalysts.

	$E_{1/2}$ (V)[a]	$E_{j=10}$ (V)[b]	ΔE (V)	*Ref.*
Ni_3Fe@FeNi-NC	**0.86**	**1.50**	**0.64**	***This work***
Fe/Ni-N-PCS	0.87	1.59	0.72	*J. Colloid Interf. Sci. 2023, 633, 828-835.*
Fe-N@CBs	0.91	1.65	0.74	*Appl. Catal. B 2025, 370, 125189.*
Fe-N_x@NSCST-ZL	0.94	1.71	0.77	*Chem. Eng. J. 2023, 471, 144515.*
FePc-CoNC-CMS	0.86	1.54	0.68	*ACS Sustain. Chem. Eng. 2024, 12, 4779-4788.*
Ru_{SA}-NiFe LDH	0.89	1.46	0.57	*Nat. Commun. 2024, 15, 9616.*
Co/Co_3O_4@N-CNTs	0.83	1.50	0.67	*Chem. Eng. J. 2022, 448, 137709.*
CoFeN-NCNTs//CCM	0.84	1.56	0.72	*Adv. Funct. Mater. 2022, 32, 2107608.*
FeCoNi@$MnAl_2O_4$-950	0.79	1.54	0.65	*J. Alloy. Compd. 2024, 1004, 175802*
Fe/Ni-NC||FeNi@G	0.89	1.50	0.61	*Electrochim. Acta 2023, 458, 142549.*
Mn-RuO_2	0.86	1.50	0.64	*J. Am. Chem. Soc. 2022, 144, 2694-2704.*
CNT@FeCo-C_3N_4 & Ni_7Fe-LDH	0.80	1.71	0.91	*J. Mater. Chem. A 2025, 13, 19821-19830.*
FePc-NiCo-LDH/Ti_3C_2	0.90	1.50	0.60	*Appl. Surf. Sci. 2022, 591, 153142.*
$NiCo_2S_2$@NiFeLDH/N-rGO	0.81	1.49	0.68	*Energy Environ. Sci. 2025, 18, 991-1001.*
LDH||PCS||Pc	0.88	1.51	0.63	*Adv. Sci. 2025, 12, e06172.*
FeNC@LDH	0.89	1.46	0.57	*Joule 2024, 8, 1-16.*

[a] Determined in O_2-saturated 0.1 M KOH solution.

[b] Determined in O_2-saturated 1.0 M KOH solution.

The ΔE value of Ni_3Fe@FeNi-NC ranks among the best reported for both single-component and multicomponent non-precious electrocatalysts.

Table S3. Comparison of liquid zinc-air battery performances between Ni_3Fe@FeNi-NC and other reported electrocatalysts.

Air Cathode	Peak power Density (mW/cm^2)	Specific capacity (mAh/g)	Cycling stability	*Ref.*
Ni_3Fe@FeNi-NC	**181**	**827 @10 mA cm^{-2}**	**850 h @10 mA cm^{-2}**	***this work***
MS-Co_{SA}-N-C-800°C	160	760 @10 mA cm^{-2}	300 cycles @10 mA cm^{-2}	*ACS Nano 2022, 16, 11944-11956.*
$NiCo_2S_2$@NiFeLDH/N-rGO	188	732 @10 mA cm^{-2}	668 @10 mA cm^{-2}	*Energy Environ. Sci. 2025, 18, 991-1001.*
CoSAs-NGST	148	-	133 h @5 mA cm^{-2}	*Adv. Funct. Mater. 2021, 31, 2010472.*
Fe/Ni-NC||FeNi@G	200	876 @10 mA cm^{-2}	500 h @5 mA cm^{-2}	*Electrochim. Acta 2023, 458, 142549.*
LDH||PCS||Pc	172	816 @5 mA cm^{-2}	300 h @5 mA cm^{-2}	*Adv. Sci. 2025, 12, e06172.*
FePc-NiCo-LDH/Ti_3C_2	148	-	80 h @10 mA cm^{-2}	*Appl. Surf. Sci. 2022, 591, 153142.*
FeCo-N-C	129	-	120 h @2 mA cm^{-2}	*Rare Met. 2023, 42, 1526-1534.*
NiOOH/P-MoS_2	125	760 @ 20 mA cm^{-2}	300 h @ 3 mA cm^{-2}	*Chem. Eng. J. 2025, 513, 162823.*
CoFeN-NCNTs//CCM	145	778 @ 10 mA cm^{-2}	445 h @ 10 mA cm^{-2}	*Adv. Funct. Mater. 2022, 32, 2107608.*
$Fe_2O(SeO_3)_2$/Fe_3C@NC	341	-	-	*Angew. Chem. Int. Ed. 2024, 63, e202412025.*
CoFe-N-C	142.1	917.4 @20 mA cm^{-2}	200 h @5 mA cm^{-2}	*Nano Lett. 2022, 22, 3392-3399.*
$(NiFe\text{-}LDH)_1/GA_{0.18}$	230	749 @10 mA cm^{-2}	100 h @10 mA cm^{-2}	*Chem. Eng. J. 2023, 458, 141492.*
Co,S-MnSe/N-rGO	235.2	782.7 @10 mA cm^{-2}	1833 h @10 mA cm^{-2}	*Adv. Funct. Mater. 2025, 2425430.*
Co/N@CNTs@CNMF-800	133	777 @10 mA cm^{-2}	190 h @10 mA cm^{-2}	*Adv. Funct. Mater. 2020, 30, 2003407.*
FePc-CoNc-CMS	147.6	631.1 @10 mA cm^{-2}	70 h @10 mA cm^{-2}	*ACS Sustain. Chem. Eng. 2024, 12, 4779-4788.*
PFePc-3	258.6	834 @50 mA cm^{-2}	1300 h @20 mA cm^{-2}	*Angew. Chem. Int. Ed. 2025, 64, e202501506.*
CoFe-FeNC	120.8	767.5 @10 mA cm^{-2}	1200 h @10 mA cm^{-2}	*Appl. Catal. B Environ. Energy 2024, 359, 124485.*

FeOM-Mo_2CT_x	155.3	796.3 @10 mA cm^{-2}	1500 h @10 mA cm^{-2}	*Adv. Funct. Mater. 2025, 35, 2422254.*

The rechargeable aqueous ZAB assembled with Ni_3Fe@FeNi-NC exhibits competitive performance, however, it remains slightly inferior to the state-of-the-art systems, primarily owing to complexities associated with device assembly.

References

[1] D. Feng, Z.-Y. Gu, J.-R. Li, H.-L. Jiang, Z. Wei, H.-C. Zhou, *Angew. Chem. Int. Ed.* **2012**, *51*, 10307-10310.

[2] M. Zhao, Y. Wang, Q. Ma, Y. Huang, X. Zhang, J. Ping, Z. Zhang, Q. Lu, Y. Yu, H. Xu, Y. Zhao, H. Zhang, *Adv. Mater.* **2015**, *27*, 7372-7378.

[3] B. Liu, B. Liang, J. Xiao, M. Feng, H. Cheng, Y. Li, Y. Cheng, K. Zhang, *Compos. Part A* **2024**, *176*, 107869.

[4] J.-N. Liu, C.-X. Zhao, J. Wang, X.-Q. Fang, C.-X. Bi, B.-Q. Li, Q. Zhang, *Joule* **2024**, *8*, 1-16.

[5] O. Bondarchuk, A. P. LaGrow, A. Kvasha, T. Thieu, E. Ayerbe, I. Urdampilleta, *Appl. Surf. Sci.* **2021**, *535*, 147699.

[6] Q. Zhang, W. Xiao, H. C. Fu, X. L. Li, J. L. Lei, H. Q. Luo, N. B. Li, *ACS Catal.* **2023**, *13*, 14975-14986.

[7] J. F. Parker, J. S. Ko, D. R. Rolison, J. W. Long, *Joule* **2018**, *2*, 2519-2527.